Geophysical Journal International

Geophys. J. Int. (2021) **224,** 985–1002
Advance Access publication 2020 October 20
GJI Geodynamics and tectonics

doi: 10.1093/gji/ggaa498

The 2018 M_w7.5 Palu 'supershear' earthquake ruptures geological fault's multisegment separated by large bends: results from integrating field measurements, LiDAR, swath bathymetry and seismic-reflection data

Danny Hilman Natawidjaja[1], Mudrik R. Daryono,[1] Gegar Prasetya,[2] Udrekh,[3] Philip L-F. Liu,[4] Nugroho Dwi Hananto,[1] Widjo Kongko,[5] Wahyu Triyoso,[6] Anggraini Rizkita Puji,[1] Irwan Meilano,[6] Endra Gunawan,[6] Pepen Supendi,[7] Astyka Pamumpuni,[6] Mashyur Irsyam,[6] Lutfi Faizal,[8] Sri Hidayati,[9] Benyamin Sapiie,[6] Mipi A. Kusuma[6] and Sukardan Tawil[10]

[1] *Indonesian Institute of Science, Indonesia. E-mail: danny.hilman@gmail.com*
[2] *Indonesian Association of Tsunami*
[3] *National Agency for Disaster Management (BNPB)*
[4] *National University of Singapore, Singapore*
[5] *Agency for The Assessments and Applications of Technology (BPPT)*
[6] *Institute of Technology Bandung, Bandung, Indonesia*
[7] *Agency for Meteorology, Climatology, and Geophysics (BMKG), Jakarta, Indonesia*
[8] *Ministry of Public Works and Housing, National Center for Earthquake Studies(PuSGeN), Bandung, Indonesia*
[9] *Geological Agency of Ministry of Mines and Energy, Center for Volcanology and Mitigation of Geological Disaster, Bandung, Indonesia*
[10] *Geology Department Palu,Tadulako University, Palu, Indonesia*

Accepted 2020 October 18. Received 2020 October 10; in original form 2020 July 7

SUMMARY

On 2018 September 28, 18:02:44 local time, the magnitude 7.5 earthquake accompanied by a tsunami and massive liquefaction devastated Palu region in Central Sulawesi, Indonesia. Comprehensive post-disaster surveys have been conducted, including field survey of surface ruptures, LiDAR, multibeam-bathymetry mapping and seismic-reflection survey. We used these data to map fault ruptures and measure offsets accurately. In contrast to previous remote-sensing studies, suggesting that the earthquake broke an immature, hidden-unknown fault inland, our research shows that it occurred on the mappable, mature geological fault line offshore. The quake ruptured 177-km long multifault segments, bypassing two large releasing bends (first offshore and second inland). The rupture onset occurred at a large fault discontinuity underwater in a transition zone from regional extensional to compressional tectonic regimes. Then, it propagated southward along the ∼110-km submarine fault line before reaching the west side of Palu City. Hence, its long submarine ruptures might trigger massive underwater landslides and significantly contribute to tsunami generation in Palu Bay. The rupture continued inland for another 67 km, showing predominantly left-lateral strike-slip up to 6 m, accompanied by a 5–10 per cent dip-slip on average. The 7 km sizeable releasing bend results in a pull-apart Palu basin. Numerous normal faults occur along the eastern margin. They cut the Quaternary sediments, and some of them ruptured during the 2018 event. Our fault-rupture map on mature straight geological fault lines allows the possible occurrence of early and persistent 'supershear', but significant asperities and barriers on segment boundaries may prohibit it.

Key words: Tsunamis; Earthquake hazards; Continental tectonics: strike-slip and transform; Neotectonics; Paleoseismology; Submarine landslides.

1 INTRODUCTION

On the 2018 September 28, the M_w 7.5 earthquake (Fig. 1a) associated with a tsunami and massive liquefaction in the Palu-bay region, Central Sulawesi, Indonesia, resulted in more than 2000 fatalities and an estimated total costs of about 22,8 trillion Indonesian Rupiahs (∼USD 1,5 billion on current-exchange rate) for rehabilitation and reconstructions, based on the report of BAPPENAS and Central Sulawesi Provincial-Government (BAPPENAS and Central-Sulawesi-Local-Government 2018). The Palukoro fault zone producing the earthquake is a west-end part of a long, fast-moving left-lateral strike-slip fault in East Indonesia. The fault begins from Papua (Yapen and Sorong Faults), through the North Molucca region (Sula-Sorong Fault) before it finally continues to Sulawesi as the Matano and Palukoro Fault (Silver *et al.* 1983; Charlton 2000; Socquet *et al.* 2006; Watkinson & Hall 2017) (Fig. 1b).

This regional east Indonesia strike-slip fault has resulted from the oblique convergence between the Pacific and Australia plates (Puntodewo *et al.* 1994; Bock *et al.* 2003). The amount of strain that partitions into left-lateral movements are up to 80 mm a^{-1}, accommodated by a 300-km wide zone focusing on the Yapen and Tarera-Aiduna fault (Watkinson & Hall 2017). Based on regional GPS data, the slip rate on the Yapen fault is 46 $\pm$ 12 mm a^{-1} (Bock *et al.* 2003), which is the indifference with the slip rate of the Matano—Palukoro fault, about 37 $\pm$ 8 mm a^{-1} (Bellier *et al.* 2001; Socquet *et al.* 2006). The age of initial movement on the Sorong fault in the Bird's head of Papua has been estimated to be about 12 Ma (million years ago) (Charlton 2000). The so-called Sula platform consisting of Paleozoic-early Mesozoic rocks (Silver *et al.* 1983) was estimated to have been left-laterally displaced about 850 km strike-slip fault from the Bird's head before it has collided with the east-arm Sulawesi (Charlton 2000). The collision resulted in the formation of the Matano and the Palukoro faults. The total offset along the Matano–Palukoro faults, based on geological reconstructions, is about 250 km (Silver *et al.* 1983). This primary strike-slip fault in Sulawesi has a tectonics role as a transform fault connecting the Tolo thrust and the Sulawesi trench, and accommodating westward-northward movement of a rigid central-Sulawesi block in a clockwise rotation driven by collision of the Sula platform in the east (Silver *et al.* 1983; Walpersdorf *et al.* 1998; Stevens *et al.* 1999; Socquet *et al.* 2006).

An advanced remote-sensing method, satellite geodesy optical-image-correlation and InSAR (Interferometric Sinthetic Aperture Radar) analysis could publish maps of surface ruptures and co-seismic displacements in just days after the event (Valkaniotis *et al.* 2018). Then, combined with the location of the main shock and the distribution of aftershocks, led to the interpretation that the initiation of the rupture broke an unknown, hidden fault, a couple of tens of km away east of the previously known *mature* geological fault line (Fang *et al.* 2019; Socquet *et al.* 2019; Song *et al.* 2019; Wang *et al.* 2019). In this scenario, the initial rupture propagated southward along the *island's neck,* then crossing the Bay and coalescing onto the principal fault zone on the Palu Bay's west side. This rupture scenario gains acceptance worldwide as used or cited in numerous literature (e.g. Muhari *et al.* 2018; Bao *et al.* ; Bradley *et al.* 2019; Carvajal *et al.* 2019; Gusman *et al.* 2019; Heidarzadeh *et al.* 2019; Patria & Putra 2020). Even though the data coverage is only partial since satellite-image data in Palu-bay water is blank; hence, there is a significant mismatch in the modelling (e.g. Song *et al.* 2019).

Besides, indications of fault movements in the *neck*, the narrow land connecting the central Sulawesi with the north-arm Sulawesi, are also hardly discernable (e.g. Wang *et al.* 2019). Therefore, the fault ruptures were thought to be buried or not quite reaching the ground surface (e.g. Bacques *et al.* 2020). This remote-sensing fault model might have misled our fundamental understanding since it allows us to consider the possibility that a massive strike-slip fault earthquake with *M*7.5 can be nucleated on and ruptured along a 70-km buried, immature (secondary) fault zone without reaching the ground surface. Unlike buried thrust faults or blind thrusts (e.g. Shaw & Suppe 1996), buried large strike-strike fault ruptures have never been observed anywhere since strike-slip fault earthquake with sizeable displacement commonly propagate to the surface (King & Wesnousky 2007).

It had also led to tsunami-source modelling misinterpretations, since it only accounts for the fault rupture that runs at a short distance underwater across the Bay (Muhari *et al.* 2018; Gusman *et al.* 2019; Heidarzadeh *et al.* 2019). Hence, it underestimates tsunami excitation due to underwater fault movements but solely attributed to (suspected) massive underwater landslides. Tsunami-wave models based on coastal landslides alone cannot explain the tsunami-wave records (Liu *et al.* 2020).

This study comprehensively integrates the results of field observations, inspections of LiDAR-data coupled with mosaic high-resolution aerial photos, and analysis of high-resolution multibeam bathymetry and seismic-reflection sections (Fig. 2). We applied standard techniques for mapping active faults based on visual inspections of tectonic landforms, such as fault scarps, linear and pressure ridges, long-straight valleys and displaced or deflected streams both for land topography and bathymetry (e.g. Yeats *et al.* 1997; Sieh & Natawidjaja 2000; Burbank & Anderson 2001). As standard in mapping, we also included liquefaction and landslide features associated with the 2018 earthquake and previous events. Hence, we provide the most complete and accurate map of active faults together with the 2018 Palu earthquake ruptures throughout the Palu region both inland and offshore (Figs 3, 4 and 6, and Figs S1 and S2a–h, Supporting Information). Detailed fault geometries and precise measurements of co-seismic slip variations provide new insight into the fault rupture kinematics and its related hazards (Fig. 6 and Table S1, Supporting Information). Our fault map can be viewed in the *Google Maps* at link: https://goo.gl/maps/pkiou8t68DVcu2YE6. We also provide the KMZ extension files of the fault lines in the e-Supplement for viewing in the *Google Earth* or others.

2 THE PALUKORO FAULT ZONE: GEOMETRY AND SEGMENTATIONS

The Palukoro fault is very segmented. We divide it into four main segments separated by large bends and stepovers, from north to south: *Tanimbaya, Donggala, Palu* and *Saluki* segments (Fig. 3). The fault regionally curves clockwise from the Tanimbaya Peninsula toward the North Sulawesi trench, resulting in a broad compressional tectonic regime that connects the strike-slip fault system to the subduction zone (Fig. 1a). Therefore, the Tanimbaya segment is the beginning of the contractional strike-slip fault regime. The Tanimbaya segment is separated from the Donggala segment in the south by a 4.2 km width restraining stepover, with secondary reverse faults as a part of flower structures along a compressional strike-slip zone (Harding 1985). The Donggala segment has a slight restraining bend in the middle (Fig. 3 and Fig. S2b, Supporting Information). The 2018 main shock location is determined at about 15 km northeast from this bend, based on the relocated main shock epicentre (Supendi *et al.* 2020).

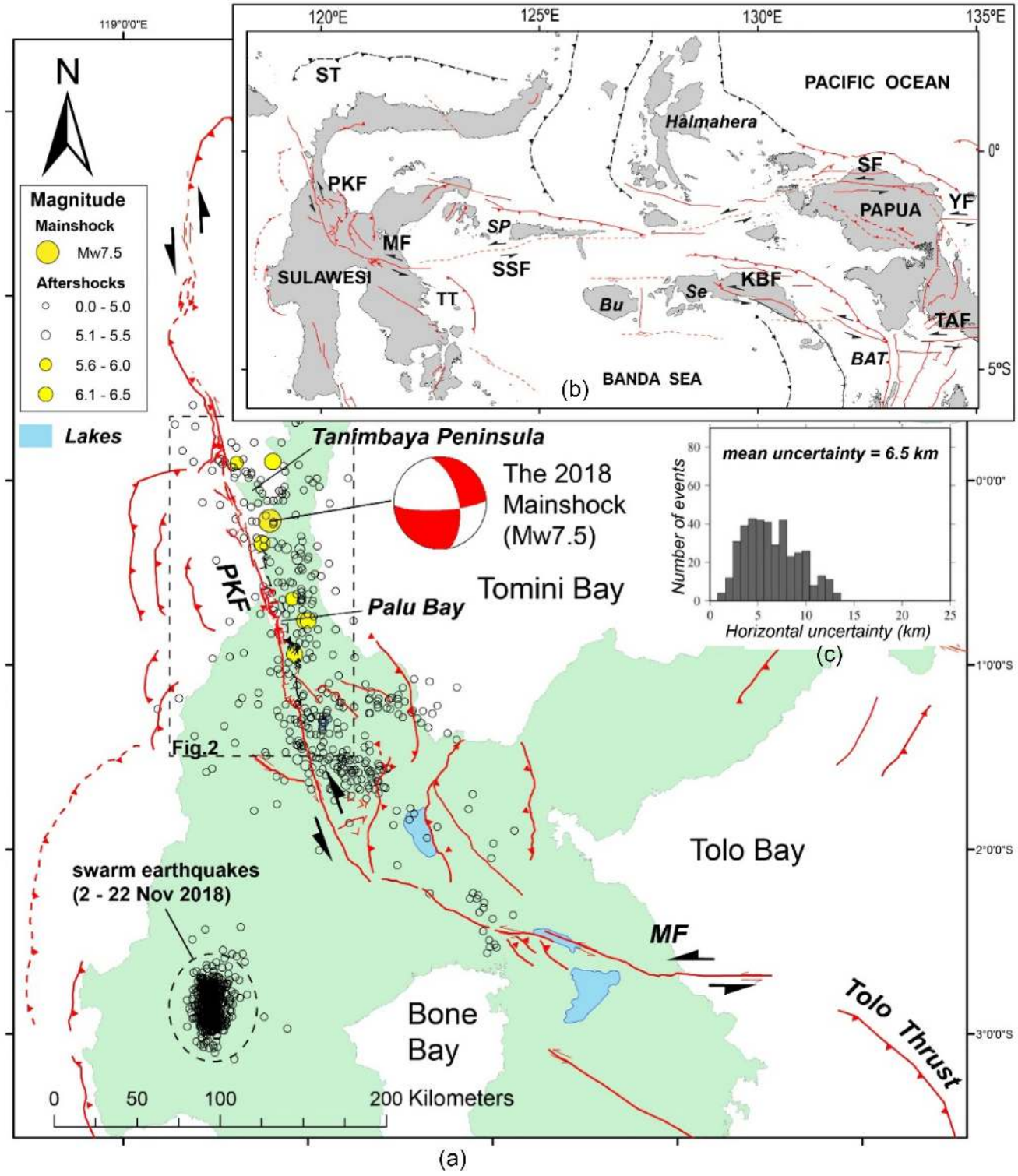

Figure 1. (a) Relocated main shock and aftershock epicentres of the 2018 earthquake from Supendi *et al.* (2020), plotted on active fault map of the Sulawesi region. (b) Index map of the regional left-lateral fault system in east Indonesia. YF = Yapen Fault, SF = Sorong Fault, SSF = Sula-Sorong Fault, TT = Tolo Thrust, MF = Matano Fault, PKF = Palukoro Fault, ST = Sulawesi Trench, TAF = Tarera-Aiduna Fault, KBF = Kawa-Boboi Fault. *SP* = Sula Platform, *BAT* = Banda-Arc Thrust, *Se* = Seram, *Bu* = Buru. (c) The relative uncertainty of epicentre relocations. The mean uncertainty is 6.5 km measured from the original position (from Supendi *et al.*, 2020).

Southward from the Tanimbaya Peninsula, the fault orientation regionally rotates eastward, implying an extensional left-lateral strike-slip fault regime. The two large releasing bends separating the fault segments marks these extensional tectonics. The first is the 3.5 km width fault bend underwater in the Palu Bay, separating the Donggala and Palu segments. The second is the 7-km width

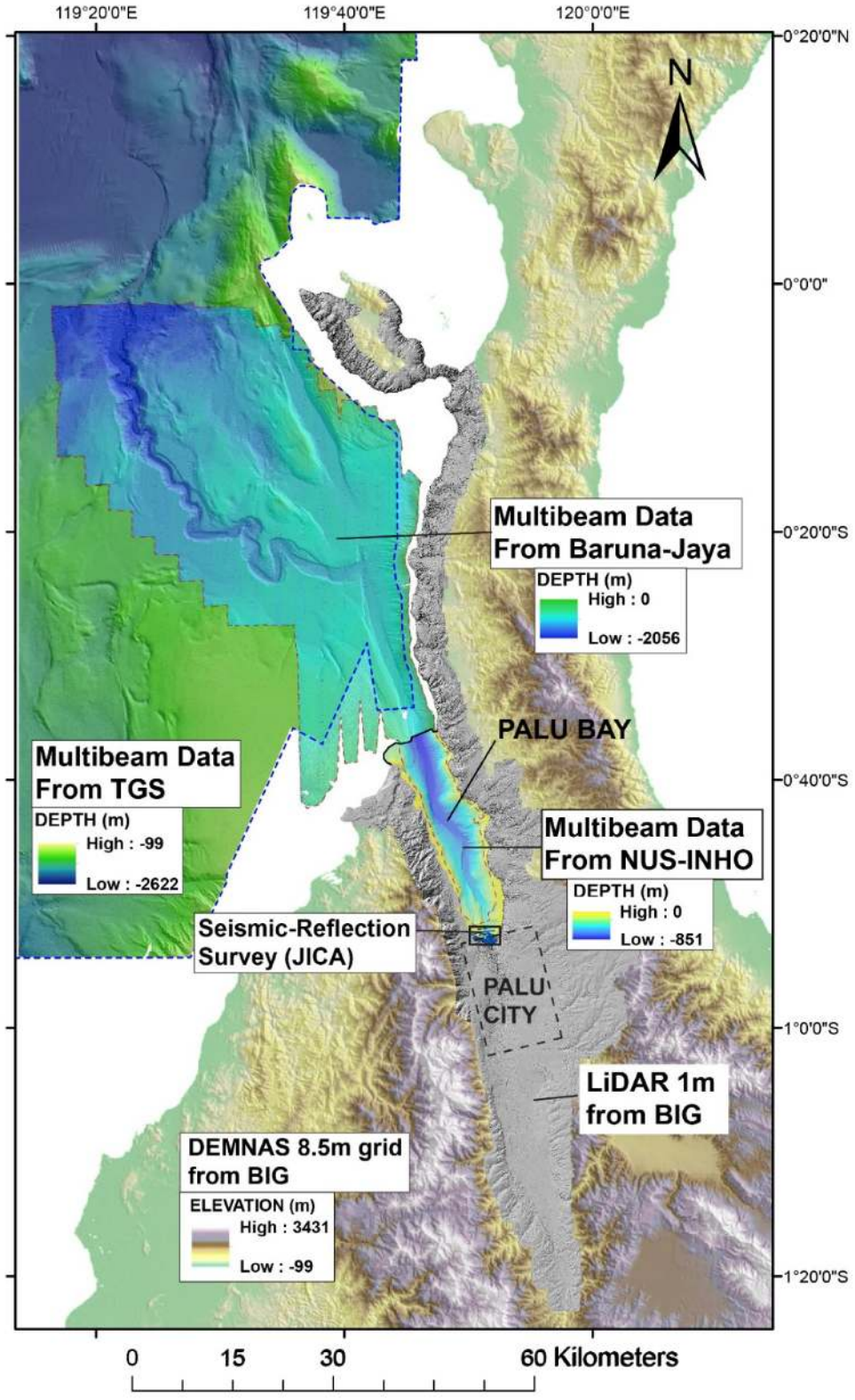

Figure 2. Index map of LiDAR coverage, various swath bathymetry data and the sparker seismic-reflection survey of JICA used in this study. The LiDAR is from the Agency of Geospatial Information of Indonesia (BIG). Swath bathymetry data are from the Baruna-Jaya survey (Frederik *et al.* 2019), the NUS-INHO (National University of Singapore—Indonesia Tsunami Society and Navy Hydrography Office) (Liu *et al.* 2020), and the old TGS data (see the text for discussions).

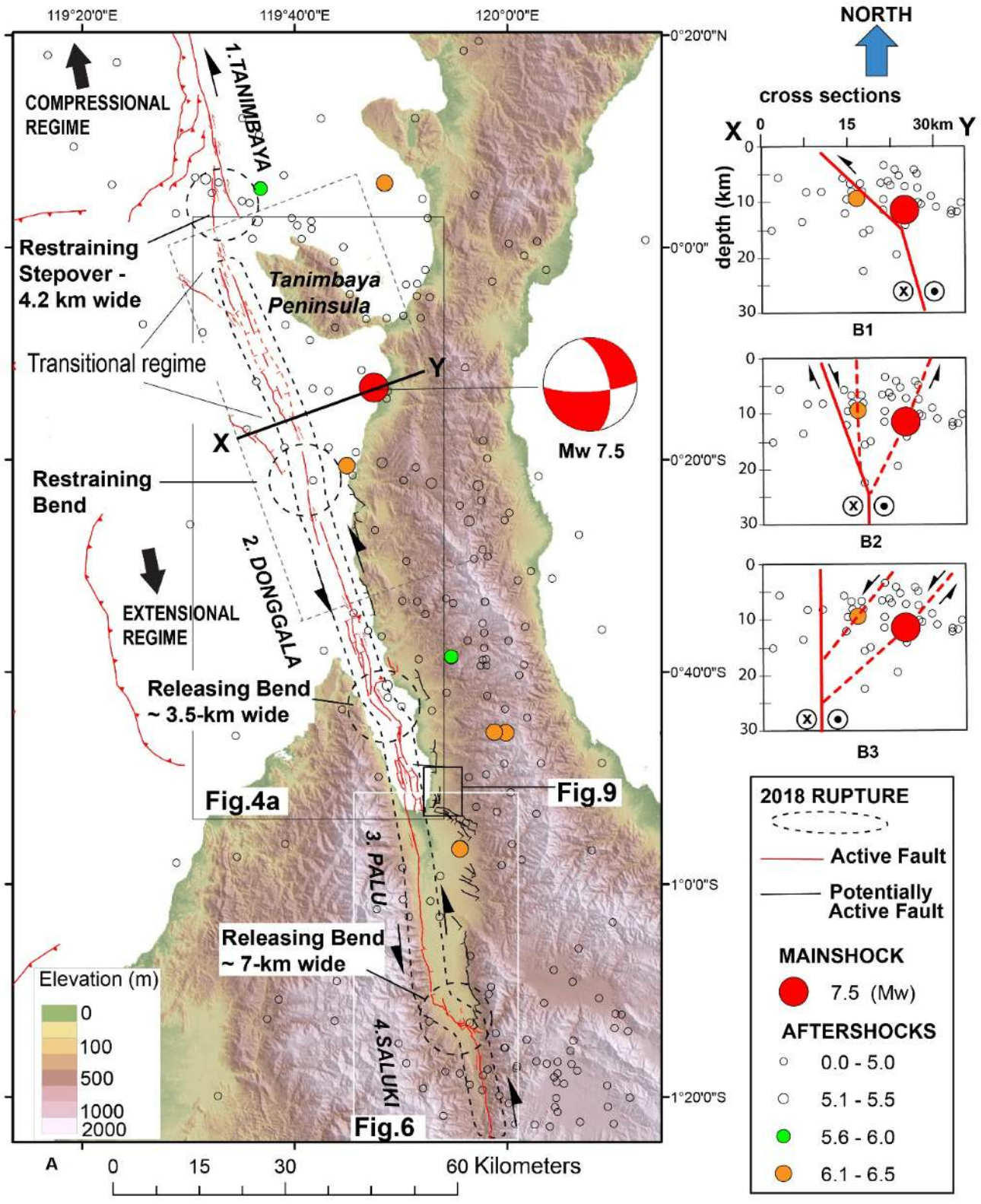

Figure 3. (a) The new map of active faults and the proposed location of the 2018 M_w7.5 ruptures from this study together with plots of the relocated main shocks and aftershocks (Supendi *et al.* 2020). Palukoro Fault divides into four segments: Tanimbaya, Donggala, Palu and Saluki. The dashed rectangle perpendicular to the *X*–*Y* line is the area of projected earthquake data. B1, B2 and B3 are plausible options of subsurface fault geometry along the *X*–*Y* cross-section concerning the main shock's location and rupture nucleation, drawn with the 2-D plots of the 2018 main shock and aftershocks (see the text for discussions).

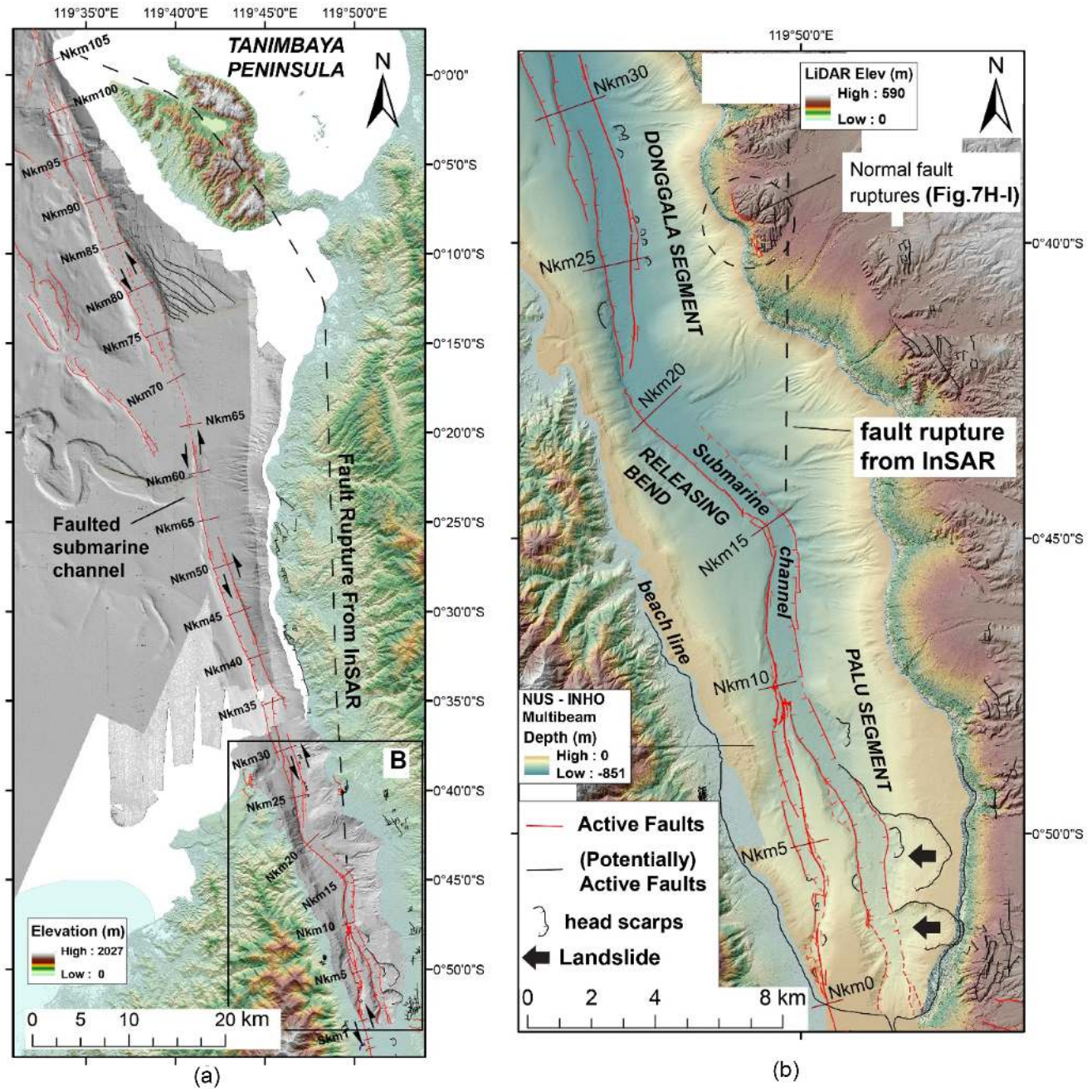

Figure 4. (a) Offshore fault lines mapped on swath bathymetry data, marked every 5 km from the Palu Beach northward. (b) Detailed active fault traces inside Palu Bay, including the presence of massive submarine landslides. The black dashed line is the inferred fault rupture deducted from InSAR (Socquet *et al.* 2019). Normal-fault ruptures occurred on the *neck* around the InSAR fault rupture, drawn as red colour lines in contrast to the rest of the black colour normal faults, denoted as potentially active faults (see the text for discussions).

bend inland, around the southern edge of the Palu pull-apart basin, separating Palu and Saluki segments (Fig. 3). Thus, the Donggala segment is in the transition zone between the compressional and extensional tectonic regimes and, hence, it is a rather complicated fault zone portraying both regimes' influence.

A broad extensional zone along the eastern margin of the Palu pull-apart basin and the west side of the neck region facilitate the extensional tectonics, as shown by numerous normal faults, mapped from the field survey and inspections of tectonic landforms on LiDAR data. Numerous open fractures and some normal faults also occurred during the main shock and aftershocks of the 2018 earthquakes. Here, the normal faults along the Palu-valley eastern margin are drawn in black lines as they are secondary slow-moving faults compared to the primary fast-moving Palukoro fault zone, drawn in red. The black-line faults are denoted here as potentially active faults (e.g. Figs 3 and 4) since we do not have clear evidence that they cut the Holocene alluvium, except those ruptured in the 2018 earthquake (Figs 4b, 7h and i and 8i and j).

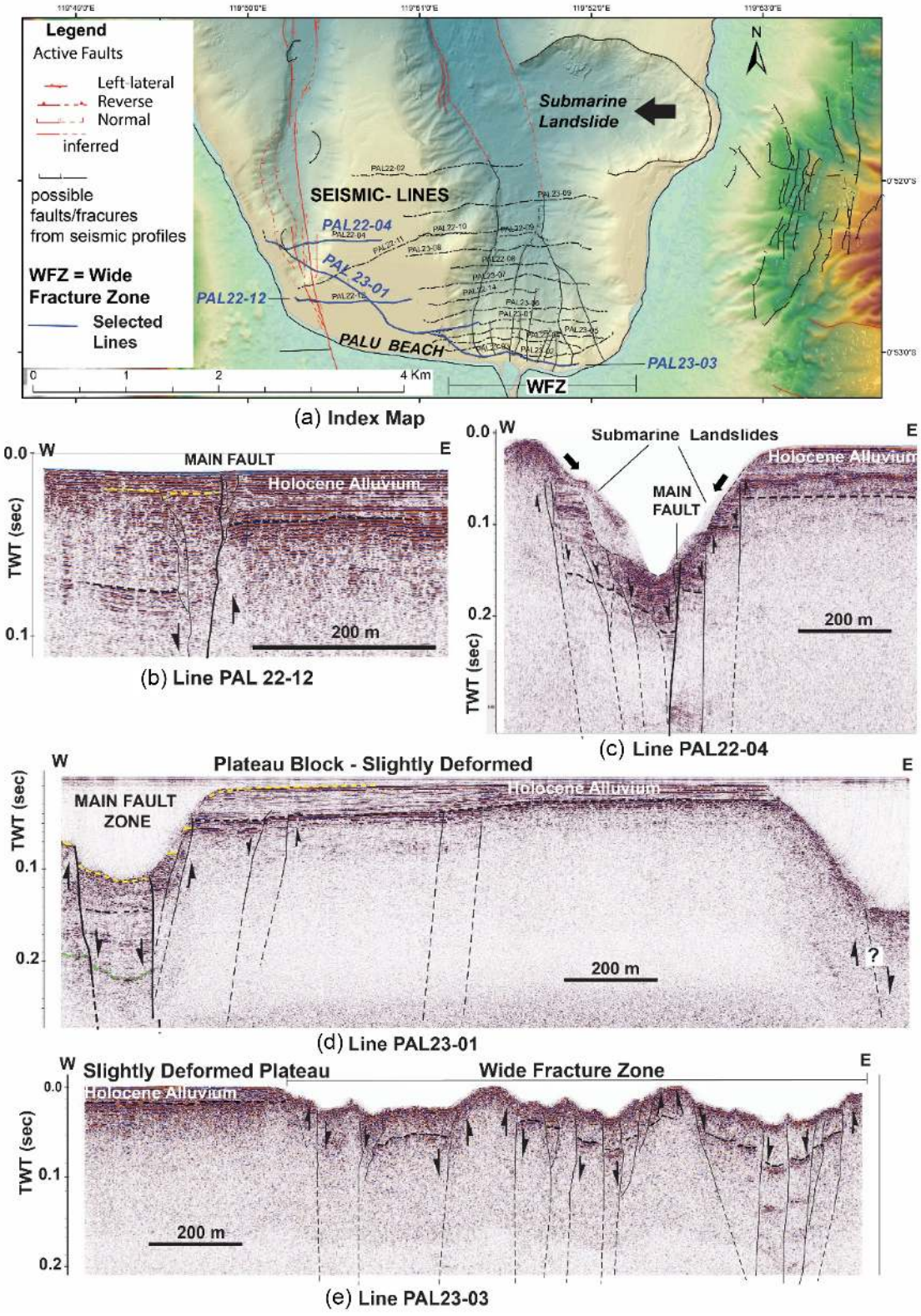

Figure 5. Sparker (single channel) seismic reflection profiles across Palu Bay. The B–E profiles have 2x vertical exaggeration, directed from west to east. The average seismic velocity is ∼1000 m/sec; hence 0.1 TWT is about 100 m. (a) Index map, (b) PAL22-12 profile showing a sharp boundary of the main fault, (c) PAL 22—04 profile showing a wide normal fault graben around the main fault, (d) PAL23-01profile is showing the principal fault zone and the slightly deformed plateau block and (e) PAL23-03 profile across the east side of the bay showing a broad zone of extensional fractures.

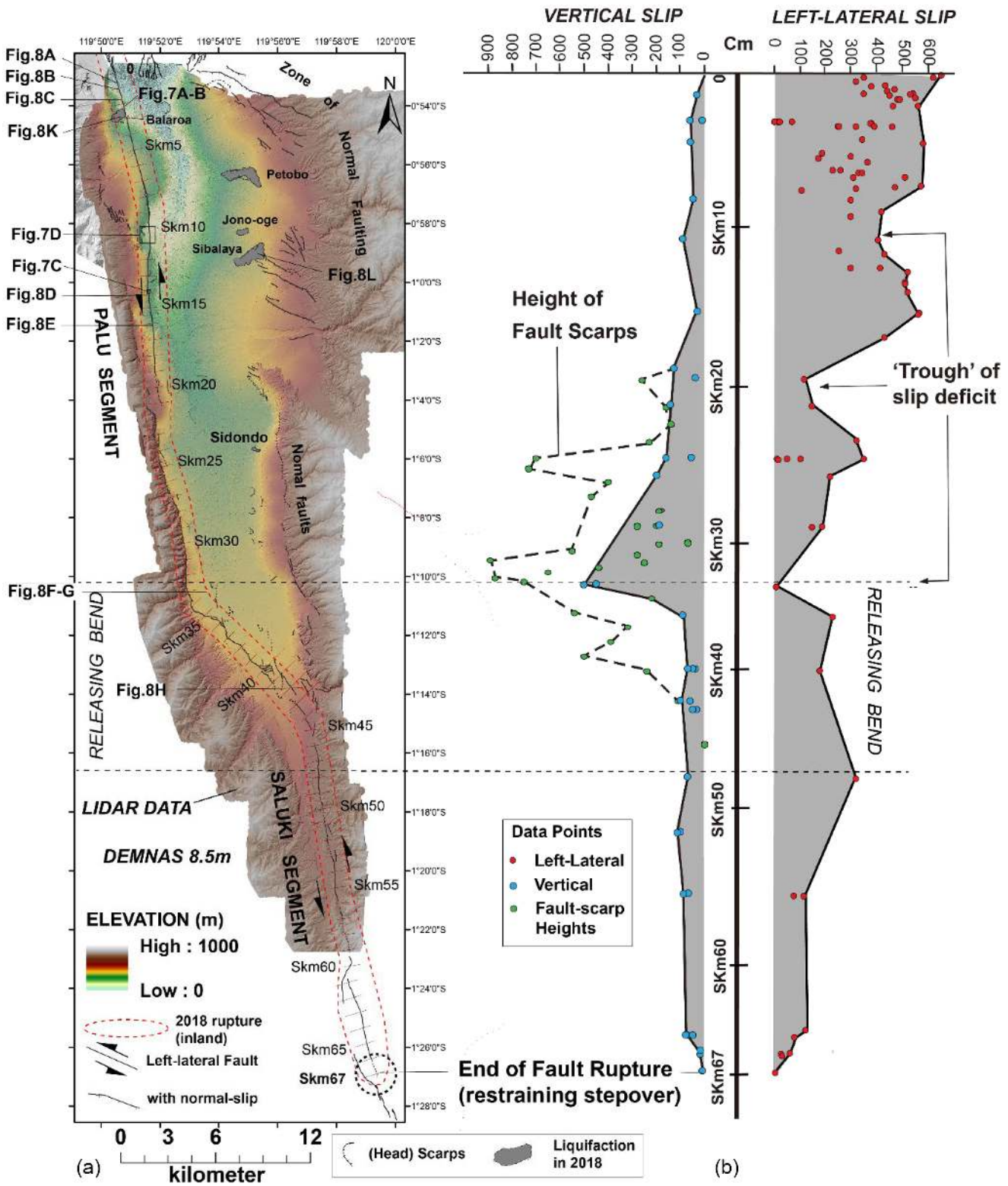

Figure 6. (a) Map of inland active fault ruptures from this study. The 2018 main ruptures occurred along the geological fault line. For descriptions, it is marked every 1km from the Palu Beach southward (Skm1, Skm2, etc.). (b) Distributions of left-lateral, and vertical (normal) slips along the ruptures. The shaded areas are under the graphical lines enveloping the offset data points. Note that normal slip increases approaching the fault bend while the left-lateral slip decreases.

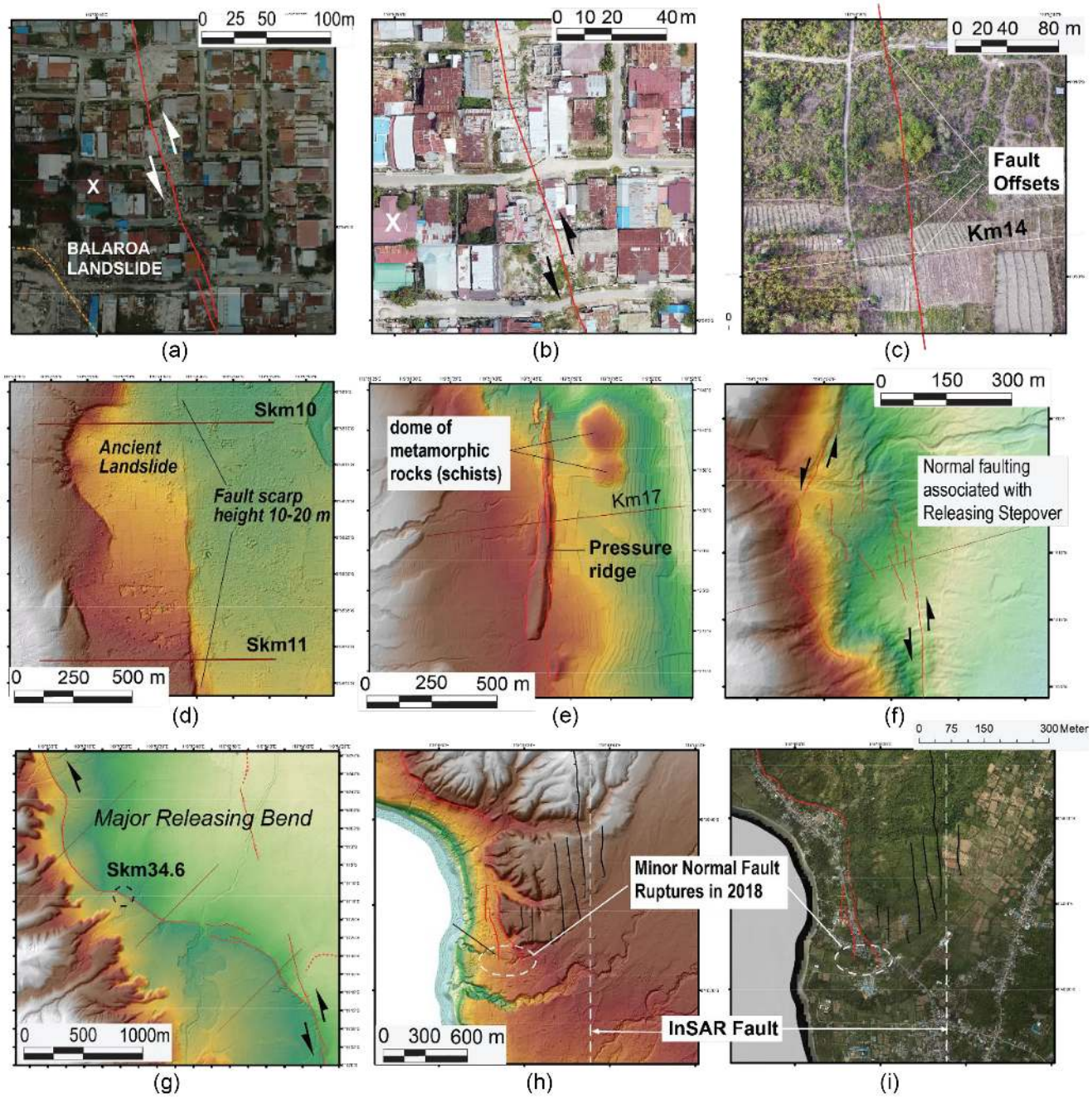

Figure 7. Illustrations of mapping methods and results. (a) Mapping surface ruptures on LiDAR orthophoto, (b) mapping surface ruptures assisted by higher resolution drone's photo, (c) an example of fault offsets of roads and paddy-field alignments on drone's orthophoto and (d) the 2018 surface ruptures along pre-existing active fault scarps seen on LiDAR DTM. Note that there is an ancient head scarp from the previous landslide hiding under heavy vegetations, (e) the 2018 ruptures along a pre-existing active fault strand associated with a pressure-ridge linear hill, (f) LiDAR DTM shows small releasing stepover associated with normal faulting, (g) mapping structural complexity around the very-large releasing bend, (h) minor normal fault ruptures around the InSAR-inferred ruptures plotted on LiDAR DTM and (e) similar map but plotted LiDAR orthophoto. Locations of figures are marked in Figs 4 and 6 (Figs S2e and c and d, Supporting Information).

3 MAPPING OFFSHORE ACTIVE FAULTS

3.1 Swath-bathymetry data and previous interpretations

There were three swath bathymetry surveys conducted after the 2018 earthquake: two deep swath bathymetry surveys (>100 m depth) inside and outside the Palu Bay and one shallow bathymetry survey inside the Palu Bay (10–200 m depth, Fig. 2). The interagency rapid-survey team conducted the first deep-water survey from 2018 October 9 to 18 using the Baruna Jaya I research vessel of BPPT (The Agency for Assessment and Application of Technology, Frederik *et al.* 2019). The vessel was equipped with a hull-mounted Hydro Sweep DS Multibeam operating at 14–16 kHz with a beam resolution of $2^\circ \times 2^\circ$ and a geo-positioning system (GPS C-NAV

Figure 8. Field photos showing examples of fault ruptures and offsets of the 2018 event. (a) Km1 + 740, (b) Km0 + 780, (c) Km1 + 037, (d) Km14 + 180, (e) Km16 + 140, (f) Km34 + 630, (g) Km34 + 630, (h) Km42 + 420, (i) and (j) on land rupture in the eastern side of Km25 seabed—northern side of Palu City, (k) Liquefaction, and land movements in Balaroa and (l) liquefaction and land movements in Sibalaya. The location of the photos are marked in Fig. 6 and Fig. S2e in the Supporting Information.

2050) and can collect data between depths of 10–11 000 m. Data were acquired using the PDS 2000 software package (Teledyne) for hydrographic surveys (www.teledyne-pds.com) and the CARIS Hips and Sips 10 software package (Teledyne) for hydrographic data processing (www.teledynecaris. com). The second-deep swath-bathymetry survey was carried out by the Indonesian Navy Hydrography Office (INHO)(*PUSHIDROSAL*) using the *KRI Spica 934* boat during 2018 October 4–10. The bathymetry data were measured using a Kongsberg EM302 echo sounder (MBES), which can collect data for water depths up to 7000 m and has a swath width of 5.5 times the depth. The horizontal resolution is 10 m, and maximum vertical uncertainties are 0.6 per cent (i.e. 5 m at 850 m water depth).

The NUS (National University of Singapore), in collaboration with IATsI (Indonesia Tsunami Society), conducted the shallow water bathymetry survey (10–200 m) inside the Palu Bay from 2018 November 27 to December 11 (Liu *et al.* 2020). This survey used an adapted fishing boat equipped with differential GPS, a single-beam echo-sounder, accelerometers and an MBES (Kongsberg EM2040C). The MBES can collect data up to 250 m water depth and has a swath width of 2 times the depth. The horizontal resolution in the near-shore survey was about 0.8 m, and vertical uncertainties range from 5 cm to a maximum of 0.4 per cent (i.e. 0.8 m at 200 m water depth). Liu *et al.* (2020) have combined the processed deep bathymetry data, provided by INHO, with the NUS shallow bathymetry survey into a single bathymetry DEM with 5-m grid data, used by this study. The multibeam data from Frederick *et al.* (2019) overlapped with Liu *et al.* (2020) inside the Palu Bay. We also use old TGS multibeam bathymetry to further map the fault zone to the Sulawesi trench associated with the active subduction zone. The TGS data outside the Palu Bay overlapped with Frederick *et al.* (2019, Fig. 2).

From the multibeam bathymetry survey results, Frederick *et al.* (2019) and Liu *et al.* (2020) have clearly shown the existence of submarine channels inside and outside the Palu Bay. The active submarine channel started from Palu river mouth, developing a braided river, and continued northward along the long-narrow submarine valley (sub) parallel to the coastline. There is also an inactive or a former channel on the west side of the active Palu delta river, which merges at the bifurcation point about 10 km north of the Palu beachfront (Frederik *et al.* 2019, Fig. 4b and Fig. S2d, Supporting Information). Outside the Palu Bay, the submarine channel continues into the deeper water. Around 0.22°–0.24° S, it developed into two channels. The first continuous along an ∼N-S strikingly straight channel or valley toward the Tanimbaya Peninsula and the second has a sharp 90° anticlockwise turn toward the Makassar strait (Frederik *et al.* 2019, Fig. 4a and Fig. S2b, Supporting Information).

Frederick *et al.* (2019) have described and concluded that the submarine-river channels along the narrow graben associated with the offshore continuation of the Palukoro fault zone inside the Palu Bay and outside the Bay toward the Tanimbaya Peninsula. Accordingly, these fault-bounded submarine channels tend to be straight, so they have a low sinuosity index closer to 1. The sinuosity index of the channel attributes to the influenced of the alluvial fans surrounding the Bay. In contrast, the second deeper water channel that turns 90° toward the Makassar Strait develops a meandering river and has a high sinuosity of 1.7, suggesting less influence by fault (Frederik *et al.* 2019) as it flows away from the Palukoro fault zone according to our fault map. However, Frederick *et al.* (2019) did not provide the details of submarine active fault traces. Liu *et al.* (2020) also did not analyse and discuss the tectonic aspects of the multibeam bathymetry but focused on mapping and quantifying submarine landslides that significantly contributed to the destructive tsunami.

3.2 Fault analysis of swath bathymetry

The traces of active submarine faults reveal their tectonic landscapes on the high-resolution bathymetry (Fig. 4 and Figs S2a–d, e-Supplement 1, Supporting Information). However, identifying the 2018 fault ruptures from the available bathymetry data (i.e. ≥5-m grid DEM) is impossible because of insufficient resolution. Close to the fault lines, arcuate head scarps mark numerous submarine landslides with a radius of a couple of hundred meters to as large as a couple of kilometres wide. Some of them have fresh scarps indicating their possible relations with the recent 2018 event. The two most massive fresh submarine head scarps with radius 1.5 and 2.5 km occurred inside Palu Bay (Liu *et al.* 2020, Fig. 4b, and Fig. S2d, e-Supplement 2, Supporting Information).

For the ease of descriptions, we put 5-km interval marks along the offshore fault zone from the Palu-City beach northward with notations Nkm5, Nkm10, etc. (Fig. 4, and Figs S2a–d, e-Supplement 3, Supporting Information). From Nkm90 on the northern Donggala segment northward to Nkm105, the fault runs into ∼ 4.2 km width restraining stepover, marked by the closing of its associated submarine long-narrow graben valley. From Nkm90 southward to Nkm70, the fault zone is marked by a narrow, straight submarine graben with a width up to 2700 m at depth about ∼1000 m. From Nkm70 to NKm50, the fault swings clockwise before returns to the initial trend along Nkm50 to Nkm35. Hence, it forms a restraining bend, marked by disappearing and re-appearing of the submarine channel or graben. This bend separates the northern and southern parts of the Donggala segments.

Between Nkm 60–55, a primary fault trace, associated with fresh-looking sharp-linear fault scarps facing east, runs in the front of the 1500-m submarine channel that turns sharp 90° to the west. Here, we suggest that the submarine channel might initially flow northward. Since the restraining bend has uplifted the area between Nkm60–70, then the submarine channel flow has been blocked and deflected to the west (Fig. 4a, and Fig. S2b, Supporting Information). From Nkm60 southward, the long-narrow submarine channel or graben re-appears and continues very straight until reaching Nkm20. From Nkm20 to Nkm15, the submarine channel sharply bends eastward, interpreted as the 3.5 km width releasing fault bend, associated with predominated normal faulting.

From Nkm15 toward the beach (Nkm0), the fault-controlled submarine channel is relatively straight, but it bifurcates into two at Nkm10. The larger eastern channel goes to the mouth of the active Palu River, and the western smaller channel runs toward the location of the 2018 main fault rupture, located close to the western margin of the Palu valley (Fig. 4b, and Fig. S2d, Supporting Information). The fault movement has uplifted the western submarine channel relative to the main eastern channel, leaving it as a hanging submarine channel no longer active (Fig. 4b, and Fig. S2d, Supporting Information).

3.3 Fault analysis of seismic-reflection profiles

PT HGS (Hydro Geophysical Survey) conducted the single-channel seismic-reflection survey under Japan International Corporation Agency (JICA) and The National Agency for Planning and Development (BAPENNAS) project. The survey used seismic energy source CSP-D2400, Applied Acoustics Squid 2000 Sparker with floats, single-channel 8 hydrophone streamer, and CODA DA2000 data recording system suitable for a local-wooden boat equipped with a 7.5 KW 220 V generator. Data acquisitions use a 1.2 s shotpoint interval at ∼1 m s^{-1} vessel speed with a sampling rate of 8 kHz. Streamer and sparker tow-depth are approximately 0.3 and 0.2 m. Data processing includes deconvolution and filtering, calculation of the CDP positions, geometry corrections and bandpass filter at 400–2000 Hz 24 dB/octave and IIR Zero phase filter. The positioning during mobilization in Palu used the Trimble GPS SPS 461 and heading with Marine Star signal HPG 2 with 10 m accuracy.

To help detailed interpretation in this study, we conducted advanced seismic data processing to reduce noises and enhance signals based on the raw seismic data. The aim is to improve the coherence of signal quality. Furthermore, several preconditions are carried out, such as *FX deconvolution* and *amplitude balancing* to improve coherence and continuity. Based on our filter test, the signal bandwidth is in the range of 250–500–1250–2500 Hz, and the better coherence and continuity resulted after predictive deconvolution with the bandpass filter of about 250–500–750–1250 Hz. We exercised the step of *predictive deconvolution* and several parameters of *Gap and Operator Length*. It appears the optimum predictive deconvolution parameter with the Gap = 1 and OL = 140. It is probably related to the relatively high bandwidth of the data.

To develop the velocity model, first, we do the simulation seismic migration based on the single velocity model (110 per cent, 105 per cent, 100 per cent, 95 per cent and 90 per cent) on the default ProMAX marine seismic velocity model. The 95 per cent velocity

model appears to be good enough. The next step is constructing a straightforward interpretation and lumping the simple velocity model based on the seismic horizon interpretation. Then, to collapse the diffractions, we use this simple velocity model for the *Kirchhoff method* of the seismic migration process. Finally, we conducted a geological interpretation of the enhanced seismic-reflection profiles across the Palu-City Bay Front to identify subsurface structures related to the 2018 fault ruptures and local tectonics (Fig. 5). Together with high-resolution bathymetry data, we mapped the continuation of the inland fault rupture lines into Palu Bay.

We interpret that from NKm10 southward, where the submarine channel splits into western and eastern channels, the Palukoro-fault graben widens. The western smaller linear graben representing the negative-flower-structure becomes narrower and disappears toward the beachfront. From the beachfront southward, the fault formed a sharp straight line. This gradual change correlates well with the subsurface geological structures captured by the seismic-reflection profiles, PAL22-04 (Fig. 5c), PAL23-01 (Fig. 5d) and PAL22-12 (Fig. 5b). Hence, it shows the reliability of fault mapping from morphological expressions (on bathymetry or topography).

The eastern longitudinal graben runs to the east side of the Palu valley and correlates with a wide graben with irregular sea-bottom topography shown in the east end of the Line PAL23-01 and Pal23-03 seismic sections (Figs 5d and e). The wide graben's subsurface structures on the east side are generally fuzzy because of high noises. However, the irregular topography appears to correlate with the underlying fracture zones. This subsurface broad fracture zone also coincides with abundant fractures and open fissures observed on the alluvial plain after the 2018 event. The broad fracture zones might also correlate with numerous normal faults trending N-S and NW-SE along the eastern margin and the neck land's west side. Hence, overall, the seismic-reflection profiles across the bay show three main structural features (from west to east): (1) the main fault zone on the west side; (2) the plateau block that only slightly deformed in the middle and (3) the broad fracture zones facilitating the ongoing tectonic subsidence of the eastern side of the Palu pull-apart basin.

3.4 Synthesis

Our geomorphological analysis on the high-resolution bathymetry inside and outside the Palu Bay, coupled with interpretations of single-channel seismic sections near the mouth of the Bay, has identified the continuations of the Palukoro main fault zone and its associated secondary normal faults into the Bay. It runs northward continuously underwater toward the west side of the Tanimbaya Peninsula and still goes further north, approaching the western end of the Sulawesi trench. The fresh-looking fault scarps bounded the long-straight-narrow submarine valleys represent the main fault and associated negative flower structure (normal-fault graben). Sharp linear valley and ridges and fault scarps on the seafloors reveal individual fault traces.

The plot of the remote-sensing inferred fault rupture from previous studies (Socquet *et al.* 2019), the so-called PSN (Palukoro Sulawesi Neck) Fault (Bacques *et al.* 2020), is not confirmed by any morphological evidence on the multibeam bathymetry related to fault movements (Fig. 4b, and Fig. S2c, Supporting Information). Similarly, its continuation on to the neck land is also not confirmed by fault-related landscapes as analysed from LiDAR DTM as well as from field observations. Instead, we only found minor normal-fault ruptures with a few tens of centimetres dip slip and less than 10 cm left-lateral slip inland near the location of the proposed PSN fault (Figs 4b, 7h and 8i and j, and Fig. S2c, Supporting Information).

Hence, in contrast to the previous studies postulating the 2018 rupture was nucleated on an unmappable, immature fault line beneath the island's neck (Bao *et al.* 2019; Socquet *et al.* 2019), we propose that the 2018 Palu earthquake nucleated on the mature geological fault, that is, the Donggala segment. There are several plausible explanations for the main shock epicentre being somewhat off the surface fault trace, listed according to preference.

First, since all of the large aftershocks occurred on the east of the fault zone (Supendi *et al.* 2020), epicentre determination might have been systematically shifted eastward, which, for example, could be caused by inaccuracy of the used seismic velocity model. Supendi *et al.* (2020) used 26 BMKG broadband seismic stations throughout Sulawesi and four stations along the east side of Kalimantan. Most of the stations sit on the east side of the epicentre. Their velocity model is from Widiyantoro & van der Hilst (1997) with a regional one-degree grid 3-D velocity model; Hence, it serves like a 1-D model, which might not be suitable for a complex 3-D geological structures. Moreover, the determination of the main shock and aftershock locations have average uncertainty of about 6.5 km, measured relatively from the original locations; hence it is not the absolute uncertainty (Supendi *et al.* 2020).

Second, the fault plane may dip eastward as inferred from broadband seismic data (Fang *et al.* 2019; Supendi *et al.* 2020) so that the projection of the epicentre location is on the main fault (Fig. 3-b1). However, assuming the main shock epicentre is accurate, the fault shall dip up to 45°, which is unrealistic for a strike-slip fault. Third, the fault zone has a sizeable negative flower structure (Harding 1985), as mapped in this study. Hence its secondary fault branch might lie beneath the main-shock epicentre location (Fig. 3-b2) so that the earthquake might become first nucleated on the fault branch before it propagated to the central fault plane. The fourth is like the third reason but assuming a more vertical main fault offshore (Fig. 3-b3).

4 MAPPING INLAND FAULT RUPTURES AND OFFSETS

The survey for acquiring the LiDAR data set, including DTM, DSM and orthophoto, was conducted between 2018 mid-November and 2019 January by the Agency for Geospatial Information (BIG). LiDAR data covers about 2 million km^2 areas around the Palu Bay (Fig. 1) with an accuracy of the 1-m grid. The associated orthophoto has a pixel resolution of 10 cm. For mapping fault outside the LiDAR coverage, we use DEMNAS, Indonesian DEM with 8.5 m grid data, provided by BIG and freely available at http://tides.big.go.id/DEMNAS/.

We conducted the inland field surveys in two campaigns. The first fieldwork was in 2018 October, a few weeks after the event, as part of PuSGeN (National Center for Earthquake Studies)'s activities under the Ministry of Public Works and Housing (PuSGeN 2018, 2019). The second fieldwork was conducted in 2020 January, supported by the JICA as part of the 'Building Back Better Palu Region After the 2018 Disaster' (https://undpindonesia.exposure.co/palu-central-sulawesi-building-back-better).

We mapped fault ruptures and measured lateral and vertical offsets with measuring tapes, geological compass and hand-held GPS. Before, during, and after field surveys, we conducted visual inspections of LiDAR DTM, DSM, and associated orthophoto using GIS software. During the fieldwork, we also conducted an aerial survey

using a small UAV (Unmanned Aerial Vehicle) quadruple drone, enabling us to develop higher resolution orthophoto (i.e. ∼3 cm pixel resolution) and DEM (Digital Elevation Model) as complementary to the LiDAR data set. Hence, we have comprehensive documentation of fault ruptures, including associated horizontal and vertical offsets. The result is shown in Fig. 6(a). Larger scale maps are provided in Supporting Information (Figs S2e–h, e-Supplement 4 and e-Supplement 5). To improve clarity, we put 1-km interval marks for the fault ruptures south of the Palu Beach with notation Skm1, Skm2, etc.

The fault ruptures run NNW-SSE to N-S across several alluvial fans in the front of the slope breaks along the mountainous western edge. From the beach, Skm0, to Skm21, the ruptures mostly occurred in sharp fault lines with clear 4–6 m left-lateral slip as measured from offsets of artificial structures, including roads, fences and house linings traces (e.g. Figs 7a–c and 8a–e, Table S1, Supporting Information). From Skm0, the rupture orientation is NNW-SSE, but from Skm8, it slightly swings westward and becomes almost N-S until Skm21. Massive liquefaction and landslide occurred in Balaroa area between Skm2 and Skm3 (Figs 6a and 8k, and Fig. S2e, Supporting Information). The arcuate head scarps diameter is about 500 m, and the longitudinal length of the slide is ∼ 900 m. The toes of the landslide lie right on the west side of fault ruptures.

Interestingly, the surface ruptures along the front of the toes did not occur as a single primary fault line like its north and south sides but locally disperse into several lines within a few-hundred-metres zone. The Balaroa liquefaction zone occurred just next to the broad alluvial fan's northern edge between Skm2–Skm10 (Fig. S2e, Supporting Information). Note that the liquefaction occurred in the area of a housing estate; it is not associated with any irrigation canal like in Sibalaya (Fig. 8l, e-Supplement 2) or a paddy field as suggested to play a significant role in liquefaction (Bradley *et al.* 2019; Cummins 2019; Watkinson & Hall 2019).

Around Skm10, there is an ancient head scarp of comparable size, probably occurred during a previous earthquake event (Fig. 7d, and Fig. S2e, Supporting Information). Hence, the previous liquefaction and landslides did not occur at the same place; so, it might also occur in different spots in the future. Hence, ascribing liquefaction hazard zones for the future should take this evidence into account for further evaluations. Around Skm10–11, we mapped a very-straight fault scarp on alluvial plain hidden under heavy vegetations but revealed on LiDAR DTM (Fig. 7d). The scarps' height is between 10–20 m with east-side down, testifying significant dip-slip movements. Around Skm17, there is a spectacular linear pressure ridge on the Holocene alluvial fan (Fig. 7e). Behind it are peculiar twin domes underlying by metamorphic rocks (schists).

From Skm21 to Skm25, the fault ruptures shift toward the hill slope forming a 1-km wide restraining stepover. However, southward, the rupture shifted back toward the east, forming a smaller releasing stepover, accompanied by numerous normal faulting (Fig. 7f). The fault lines rotate back to NNW-SSE direction, running along the slope breaks indicating a significant amount of normal-dip slips (Fig. 6a, and Fig. S2f, Supporting Information). A minor releasing bend occurred around Skm27–28, accompanied by intensive extensional fractures and normal faulting on the east side of the main rupture (Figs 6a and 7f, and Fig. S2f, Supporting Information). From Skm28 southward to Skm32, the rupture line's orientation slightly rotated back to a more northerly direction. In the eastern margin, a significant landscape change occurred, where the mountainous ridge shifted westward; hence, the Palu basin becomes narrower from latitude Skm19 southward (Fig. 6a, and Figs S2e and f, Supporting Information). Accordingly, the zone of predominantly normal faults along the eastern margin also shifts westward to around the N-S ridge slope breaks. The massive liquefaction occurred in Sidondo around the alluvial fan's toes that came from the mountain ridge (Fig. 6a, and Fig. S2f, Supporting Information).

From Skm33 to Skm45, the ruptures propagate through the 12 km NW-SE releasing fault bend, dominated by normal faulting (Figs 6a, 7g and 8f and g, and Fig. S2g, Supporting Information). In two places between Skm 36–37 and Skm 40–41, secondary strike-slip faults displaced the primary rupture zone left-laterally. Prominent normal fault scarps occurred from SKm33 to SKm40. The largest normal-dip slip occurred at Skm34–35 showing a vertical displacement of 5 m (Figs 8f and g). Around Skm40, it spreads into several branching splay faults that curve away from the main strike anticlockwise as concordance with left-lateral shear movement. The curving fault splay is a classic feature of the so-called a *horse-tail splay* that commonly marks the endpoint of strike-slip fault in a brittle medium. On the eastern margin, the mountainous ridge front cutting by normal faults shifts westward again in correlation with the sudden turn of the fault-rupture around the northern end of the fault bend between Skm34–35 (Fig. 6a, and Fig. S2g, Supporting Information). From Skm45 southward, the fault rupture line swings back to the initial NNW-SSE orientation up to the end of the rupture around Skm67 at a 1.5-km wide restraining stepover (Fig. 6a, and Figs S2g and h, Supporting Information).

We combined direct measurements of fault offsets in the field and analyses from LiDAR orthophoto, DTM, DSM, mosaic aerial photographs and higher resolution DEM developed from UAV surveys (Table S1, Supporting Information). The existence of many human-made infrastructure alignments of (asphalt) roads, bricked fences, buildings and field-rice boundaries, which were cut by the fault ruptures, provide excellent markers for offset measurements (Figs 7a–c and 8a–j).

The left-lateral slip slightly decreases from Skm0 to Skm15, but with a significant slip deficit between Skm7 and Skm12.5 (showing as a 'trough' in Fig. 6b), interestingly coincides with the location of a massive ancient landslide in Sibedi (Fig. 6a, and Fig. S2e, Supporting Information). Fault slips are not pure strike-slip but are accompanied by dip-slip of a few tens of centimetres up to 1 m, mostly east down. The significant dip-slip movement relates to a prominent fault scarp with 10–20 m high around Skm10–11 (Fig. 7d). From Skm15 toward the south, the left-lateral slip steeply decreases, accompanied by a steady increase in dip slip. The increasing dip-slip concurs with the restraining stepover and the westward shift of the fault-rupture strands onto the mountain slope breaks at Skm22. Hence, the rate of vertical fault movement exceeds the rate of erosions and sedimentations. The restraining stepover also coincides with the trough of the left-lateral slip deficit (Fig. 6b).

The left-lateral slip goes to zero at Skm34.6, coinciding with the maximum vertical displacement of ∼5 m around the fault bend (Figs 6, 7g and 8f and g). Large dip-slip sharply decreases southeastward and returns to the average background value at Skm37, coinciding with secondary strike-slip faults tearing the normal fault lines. Concurrently, the left-lateral slip picks up, reaches ∼2 m offset at Skm37; it increases toward the southend of fault bend at SKm46 and continues southward along with the Saluki fault segments, culminating at Skm49 with ∼320 cm offset. From Skm49 southward, the left-lateral-slip gradually decreases to 100 cm at Skm66, before it disappears around Skm67 at a 1.5-km wide restraining stepover.

5 THE PALU PULL-APART BASIN

This study shows that the 2018 Palu earthquake occurred along the Palukoro left-lateral strike-slip fault with large releasing bends resulting in prominent extensional tectonics. The vertical dip-slip component on the primary left-lateral faults and associated normal faults accommodate the extensional field (e.g. Figs 5c and d). Besides, numerous normal faults trending N-S and NW-SE occur along the eastern margin, characterized by their linear fault scarps (Fig. 6a, e.g. Figs 7h and i). These normal faults are classified as *potentially active faults* since they deformed the Late-Pleistocene sedimentary layers (Becker *et al.* 2005, Fig. 9). However, they might not have moved in the Holocene period since the fault traces obscure on the Holocene alluvium or inexistence. Hence, further studies are required to evaluate their level of activity or slip rates (Fig. 8). Their black colour lines on the maps express this ambiguity, noted as potentially active faults (e.g. Fig. 4b, and Fig. S2a, Supporting Information).

Nonetheless, part of the prominent N-S trending normal faults in the neck area ruptured during the 2018 earthquake, as observed (Fig. 4b, and Figs S2c and d, Supporting Information). Bellier *et al.* (2001) have dated the Late-Pleistocene sediment on the western margin using the cosmogenic dating by measuring *in situ* produced ^{10}Be concentrations in quartz boulders exposed on top of old alluvial fan surfaces. The dating yielded an age *125 ± 20 ka (kilo-annum = thousand years ago)* for the old fan (*Qp* in Fig. 9a), which indicates the time just after the highest sea level (MIS 5e). With a similar method, they also dated the age of the young alluvial fan (*Qa*). They yielded the age of *11 000 ± 2300 yr*, which indicates that its emplacement was at the beginning of the Holocene right after the end of the Last Glacial Period. The (normal) faults interpreted to deformed these two generations of the alluvial fans (Bellier *et al.* 2001).

The normal fault assemblage on the eastern margin occurred to accommodate the Palu pull-apart-basin subsidence associated with the sizeable releasing bend between the Palu and the Saluki segments. In other words, normal faults are parts of the negative flower structures (Harding 1985). The model of structural configuration is illustrated in Fig. 10(a). The cross-section across the Palu basin shows the asymmetric graben of the flower structures (Fig. 10b). Therefore, the normal faults may move accompanying the main earthquake event on the Palukoro fault producing smaller earthquakes as the aftershocks. However, they may also rupture independently in between the main event on the Palukoro Fault.

6 CONCLUSION AND DISCUSSIONS

Advanced remote-sensing technology, such as high-resolution satellite images and InSAR, is powerful to produce information on earthquake rupture zone and co-seismic displacements in an incredibly short time after the event. However, it could not cover all details, particularly without a good knowledge of local geology. Our study concludes that for the 2018 Palu earthquake rupture is nucleated and then propagated along the pre-existing, underwater geological fault lines, not on the immature, unmappable, or hidden fault that swings eastward to the Sulawesi neck, the so-called the PSN Fault as previously interpreted (Bao *et al.* 2019; Fang *et al.* 2019; Socquet *et al.* 2019).

Our study suggests that the 2018 rupture nucleated near the centre of the Donggala segment. This rupture-nucleation spot fits perfectly with seismological data showing that in the first 8 s, the rupture propagated bilaterally northward and southward. The northward propagation only reached 30 km away before being arrested (Fang *et al.* 2019), which, according to our map, is the large 4.2-km wide restraining stepover. The fact that the Donggala segment has high asperities due to the transition between the extensional and compressional tectonic regimes allows the plausible pre-existing high-stress accumulation, and, thus, might lead to rupture nucleation with a high-stress drop that generated the so-called *supershear* wave by previous studies (e.g. Socquet *et al.* 2019). There is a previous large strike-slip fault earthquake in 1968 (M_w 7.4) that also generated a large tsunami and in 1998 (M_w 6.6), occurring on Palukoro Fault just north of the Donggala segment (Prasetya *et al.* 2001; He *et al.* 2019), possibly on the Tanimbaya segment, which might contribute to increase the stress on the Donggala segment.

The rupture propagated southward broke the submarine fault lines up-to 110-km passing the 3.5-km width releasing bend, dominated by normal faulting, before reaching the Palu Beach. Thus, unlike previously thought, it implies that the long submarine fault movements with significant dip-slip component could significantly contribute to the tsunami generation. Furthermore, the fault geometry in the Palu Bay (Skm30–Skm0) is rather complicated, having large releasing bend and fault bifurcations. Hence it acts as barriers to the fast-southward rupture propagation. Thus, it could cause higher ground shaking and intense deformations that trigger massive submarine landslides and generate a large tsunami.

On land, the ruptures continued southward for almost 40 km along mostly sharp or narrow fault zone before passing the large 7-km width releasing bend fault; then, it still propagated southward for another 25 km. Hence, the 2018 earthquake subsequently ruptured the 177-km multifault segments bypassing large stepovers and bends. Fault kinematics shows a primary left-lateral slip but accompanied by a prominent 5–10 per cent dip-slip as had been generally predicted from InSAR and seismological data (Bao *et al.* 2019; Fang *et al.* 2019). Our offset measurements reveal more details of the offsets and interplay between left-lateral and dip-slip component, particularly when passing the fault bend, where the dip-slip becomes dominant.

According to the worldwide empirical relationships between the rupture length and earthquake magnitude, a 177-km fault rupture is comparable to an average of M_w 7.7 (Wells & Coopersmith 1994), so the M_w 7.5 Palu earthquake is below the average value. The fact that the 2018 rupture propagated through two large fault segment's releasing stepover, the 3.5-km width separation offshore and the 7-km width separation on land, is essential to be noted. According to data of 26 strike-slip earthquake worldwide bypassing stepovers, only a small number could pass through the 3–4 km stepover (Wesnousky 2006). None could continuously propagate through the stepover larger than 4-km wide. However, the postulate was based on the stepovers where the fault segments are not connected, not fault bends. In other words, the fault terminations posed by Wesnousky (2006) may not apply to the fault (releasing) bends. It is also important to note that the nucleation and termination of the Palu 2018 rupture are both on the restraining stepovers, where the two segments are not connected. Thus, it seems that a fault bend is less significant than a fault stepover (i.e. a complete separation of two fault segments) in prohibiting rupture propagations.

The 2018 Palu rupture was determined to have 'supershear' speed from the onset and persistently stable until the end (Bao *et al.* 2019; Fang *et al.* 2019). However, it is implausible to have been occurred on the buried, immature, undamaged fault zone (Bao *et al.* 2019). Theoretically, the supershear rupture must occur on a straight and smooth, mature fault zone (Bouchon *et al.* 2010; Das 2015). Our fault rupture map shows that the fault sections between major bends

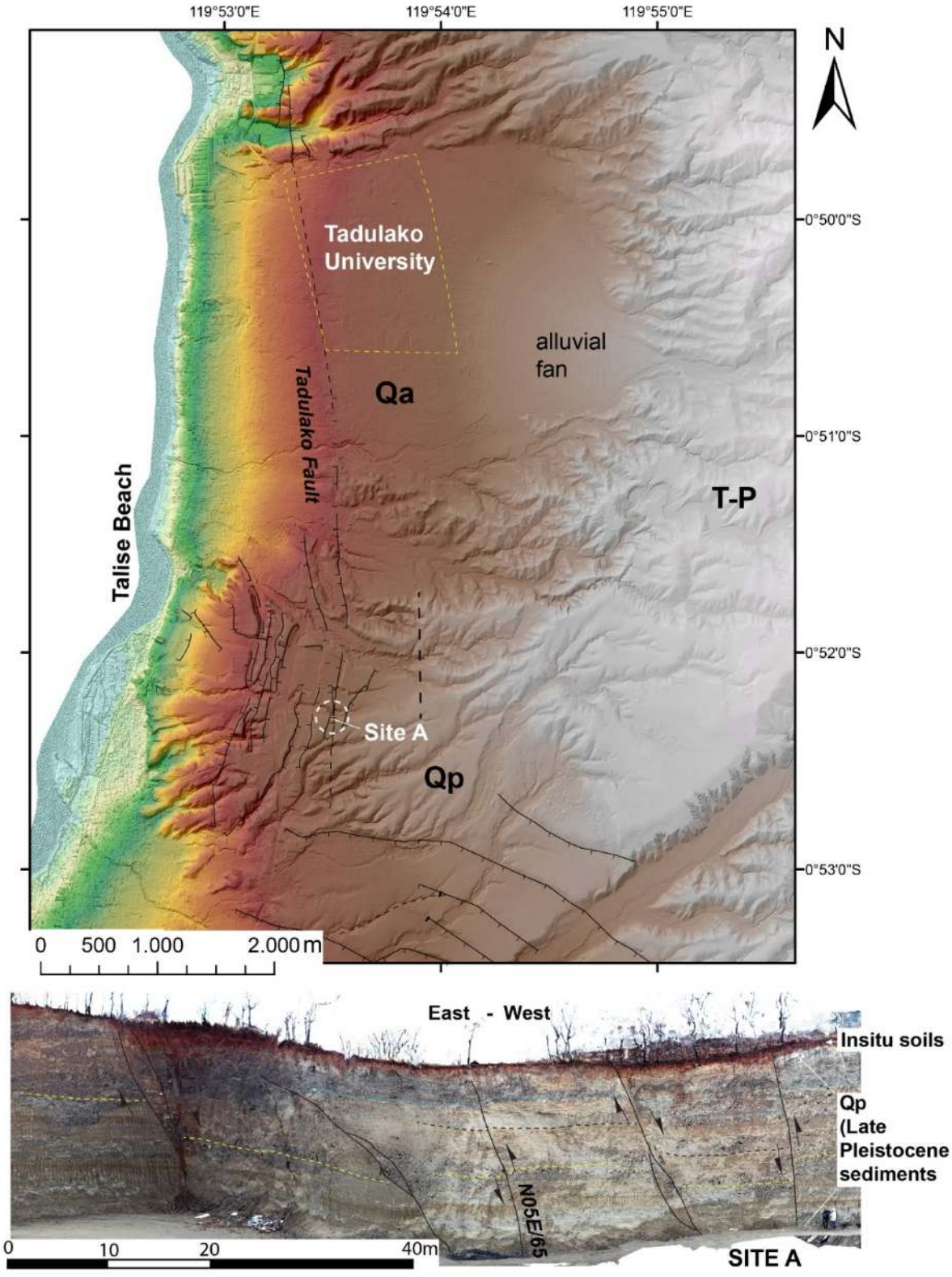

Figure 9. The upper figure is the map of normal faults trending N-S on the Talise beach in the eastern margin of the Palu depression. The lower figure is the critical outcrop showing the normal faults cutting the Late-Pleistocene sediment layers (Qp) but is obscured on the Holocene alluvial (Qa), T-P = Tertiary and Pre-Tertiary basement rocks. The location of the map is marked in Fig. 3 (Fig. S2d, Supporting Information).

are relatively simple and straight; hence, it favours the occurrence of the supershear. However, the fault discontinuities around segmentation boundaries suggests significant asperities and barriers. Therefore, the 2018 Palu supershear rupture is not so 'super' but run at ∼4.1 km s^{-1}, just a little higher than the maximum local shear wave velocity (3.4–3.8 km s^{-1}). The 2018 rupture velocity is lower

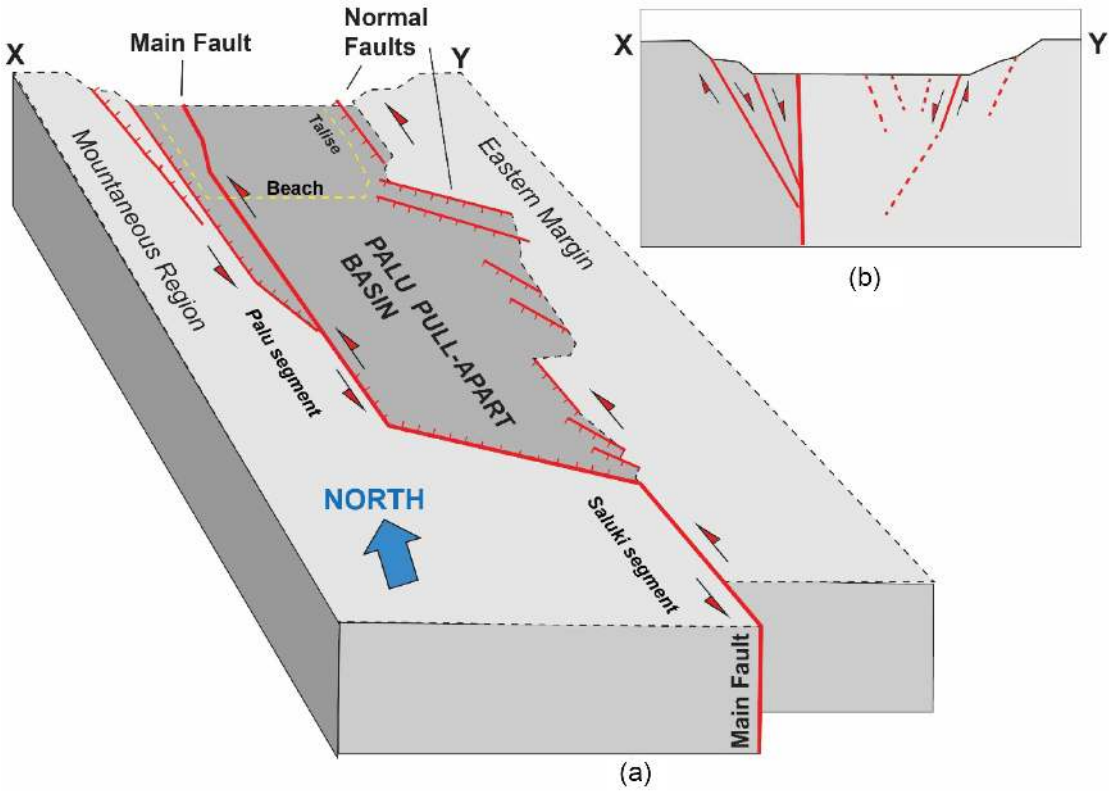

Figure 10. (a) Schematic diagram of the Palu Pull-apart structures associated with the extra-large releasing bend. (b) Schematic profile along the *X*–*Y* line.

than Eshelby's speed, the lower end of a stable supershear velocity (48–53 km s^{-1}, Bao *et al.* 2019; Fang *et al.* 2019).

SUPPORTING INFORMATION

Supplementary data are available at *GJI* online.

Figure S1. Index map of the larger-scale active fault maps in Figs S2a–h.

Figure S2. (a) Results of active fault mapping based on visual inspections of multibeam-bathymetry data around the Tanimbaya Peninsula area and plots of relocated epicentres of the 2018 main shock and aftershocks from Supendi *et al.* (2020). (b) Active fault map and plots of the relocated epicentres of the 2018 main shock and aftershocks in the area between Tanimbaya and Palu Bay. (c) Underwater fault map in the northern part of the Palu Bay and plots of the relocated epicentres of the 2018 aftershocks. The grey dashed line is the inferred fault ruptures deducted from InSAR analysis from Socquet *et al.* (2019). Note that the InSAR's fault line does not associate with any visible strike-slip fault traces on the swath bathymetry and LiDAR data; Instead, it is associated with the observed secondary normal-fault ruptures inland around Labuan. (d) Detailed subaqueous active fault map in the Palu Bayfront mapped from high-resolution bathymetry coupled with 2-D seismic reflection profiles. (e) Inland 2018 fault ruptures and active fault map in the central Palu City area from 0-km to Skm16, plotted on LiDAR DTM together with the relocated aftershock's epicentres (i.e. absence). (f) Detailed Active fault/fault-rupture map in the southern part of Palu City from Skm16 to Skm32, together with the plots of relocated aftershock's epicentres. (g) Detailed active fault/fault-rupture map around the large releasing fault bend structure, from Skm32 to Skm50 in the southernmost part of the Palu depression. (h) Detailed active fault/fault-rupture map from Skm52 to the end of the 2018 rupture around Skm67 at the 1.5 km width restraining stepover.

Table S1. Data of the offset measurements along the 2018 Palu earthquake's main rupture inland Palu Valley. The site locations are marked in Figs S2e–h.

e-Supplement 1. Undersea faults.
e-Supplement 2. Land movement.
e-Supplement 3. Northward notation KM.
e-Supplement 4. Fault rupture 2018 earthquake.
e-Supplement 5. Potentially active fault on land.
e-Supplement 6. Southward notation KM.

Please note: Oxford University Press is not responsible for the content or functionality of any supporting materials supplied by the authors. Any queries (other than missing material) should be directed to the corresponding author for the paper.

ACKNOWLEDGEMENTS

This study is funded by the CHL\R1\180173–GCRF grant from The Royal Society, UK. The fieldworks were supported and facilitated by The National Center for Earthquake study (PuSGeN), Japan International Cooperation Agency (JICA), the Ministry of Public Works, and Its Special Task Force for Palu Rehabilitation and Reconstructions, and the Central Sulawesi Province and Palu-City local governments. We are also grateful to The Agency of Geospatial Information (BIG) to develop and share the LiDAR data set. We thank all the Baruna Jaya 1 marine cruise crews and the NUS-IATsI team for their hard works and sharing the bathymetry data. We thank JICA for providing the seismic reflection data set and supporting the post-processing analysis. Finally, we appreciate

Hiroyuki Tsutsumi and Timothy Henstock for their thorough and critical reviews in improving the manuscript.

DHN is the main contributor in conceptualization, methodology, investigation, formal analysis, writing—original draft and visualization. MRD and ARP led the fault analysis based on field observations, LiDAR, orthophoto and bathymetry data, and assisted visualization. GP, PL, U and NDH conducted the multibeam bathymetry survey and provided the DEM data. WT conducted advanced processing and helped interpretations of the seismic-reflection data. PS conducted relocations of the 2018 pre-shocks, main shocks and aftershocks and provided the data. LF, MI and ST help organize and facilitate fieldwork. All authors participated in field surveys and contributed to developing and editing the manuscript.

REFERENCES

Bacques, G., de Michele, M., Foumelis, M., Raucoules, D., Lemoine, A. & Briole, P., 2020. Sentinel optical and SAR data highlights multi-segment faulting during the 2018 Palu-Sulawesi earthquake (Mw 7.5), *Sci. Rep.,* **10**(1), 1–11,.

Bao, H., Ampuero, J.-P., Meng, L., Fielding, E.J., Liang, C., Milliner, C.W.D., Feng, T. & Huang, H., 2019. Early and persistent supershear rupture of the 2018 magnitude 7.5 Palu earthquake, *Nat. Geosci.,* **12**(3), 200–205.

BAPPENAS, and Central-Sulawesi-Local-Government, 2018. *Rehabilitation and Reconstruction in Palu Area After the 2018 Earthquake (Pemulihan dan Pembangunan Kembali Wilayah Pasca Bencana Provinsi Sulawesi Tengah),* BAPPENAS (National Agency for Planning and Development).

Becker, J., Saunders, W. & Van Dissen, R.J., 2005. *Planning for The Development of Land on or close to Active Faults: A Study of the Adoption and Use of the Active Fault Guidelines,* GNS, New Zealand.

Bellier, O. *et al.*, 2001. High slip rate for a low seismicity along the Palu-Koro active fault in central Sulawesi, Indonesia, *Terra Nova,* **13,** 463–470.

Bock, Y., Prawirodirdjo, L., Genrich, J.F., Stevens, C.W., McCaffrey, R., Subarya, C., Puntodewo, S.S.O. & Calais, E., 2003. Crustal motion in Indonesia from Global Positioning System measurements, *J. geophys. Res.: Solid Earth,* **108**(B8), 2367–2389.

Bouchon, M. *et al.*, 2010. Faulting characteristics of supershear earthquakes, *Tectonophysics,* **493**(3), 244–253.

Bradley, K. *et al.*, 2019. Earthquake-triggered 2018 Palu Valley landslides enabled by wet rice cultivation, *Nat. Geosci.,* **12**(11), 935–939.

Burbank, D.W. & Anderson, R.S., 2001. *Tectonic Geomorphology,* Blackwell Science, Inc., p. 273.

Carvajal, M., Araya-Cornejo, C., Sepúlveda, I., Melnick, D. & Haase, J.S., 2019. Nearly instantaneous tsunamis following the Mw 7.5 2018 Palu earthquake, *Geophys. Res. Lett.,* **46**(10), 5117–5126.

Charlton, T.R., 2000. Tertiary evolution of the eastern Indonesia collision complex, *J. Asian Earth Sci.,* **18,** 603–631.

Cummins, P.R., 2019. Irrigation and the Palu landslides, *Nat. Geosci.,* **12,** 881–882.

, ed. Das, S. & Ansal, A., 2015. Supershear earthquake ruptures—theory, methods, laboratory experiments and fault superhighways: An update, in *Perspectives on European Earthquake Engineering and Seismology,* vol. **39,** Geotechnical, Geological and Earthquake Engineering.

Fang, J., Xu, C., Wang, S., Xu, G., Zhao, Y. & Yi, L., 2019. The 2018 Mw 7.5 Palu earthquake: a supershear rupture event constrained by InSAR and broadband regional seismograms, *Remote Sens.,* **11**(11), 1330–1345,.

Frederik, M.C.G. *et al.*, 2019. First results of a bathymetric survey of Palu Bay, Central Sulawesi, Indonesia following the Tsunamigenic Earthquake28 Septemberr 28 2018, *Pure appl. Geophys.,* **176**(8), 3277–3290.

Gusman, A., *et al.*, 2019. Source model for the Tsunami inside Palu bay following the 2018 Palu earthquake, Indonesia, *Geophys. Res. Lett,* **46,** 15, 8721–8730,.

Harding, T.P., 1985. Seismic characteristics and identifications of negative flower structures, positive flower structures, and positive structural inversion, *Bull. Am. Assoc. Petrol. Geol.,* **69**(4), 582–600.

He, L., Feng, G., Li, Z., Feng, Z., Gao, H. & Wu, X., 2019. Source parameters and slip distribution of the 2018 Mw 7.5 Palu, Indonesia earthquake estimated from space-based geodesy, *Tectonophysics,* **772,** 228216.

Heidarzadeh, M., Muhari, A. & Wijanarto, A.B., 2019. Insights on the source of 28 Septemberr 28 2018 Sulawesi Tsunami, Indonesia based on spectral analyses and numerical simulations, *Pure appl. Geophys.,* **176**(1), 25–43.

King, G.C.P. & Wesnousky, S.G., 2007. Scaling of fault parameters for continental strike-slip earthquake, *Bull. seism. Soc. Am.,* **97**(6), 1833–1840.

Liu, P.L.F., Higuera, P., Husrin, S., Prasetya, G.S., Prihantono, J., Diastomo, H., Pryambodo, D.G. & Susmoro, H., 2020. Coastal landslides in Palu Bay during 2018 Sulawesi earthquake and tsunami, *Landslides,* **17**(9), 2085–2098.

Muhari, A., Imamura, F., Arikawa, T. & Afriyanto, B., 2018. *Finding of the Unexpected Tsunami due to the Strike-Slip Fault at Central Sulawesi, Indonesia28 Septemberr 28 2018, from the Preliminary Field Survey at Palu,* Tohoku Universty, Japan.

Muhari, A., Imamura, F., Arikawa, T., Hakim, A.R. & Afriyanto, B., 2018. Solving the puzzle of the September 2018 Palu, Indonesia, Tsunami mystery: clues from the Tsunami waveform and the initial field survey data, *J. Disaster Res.,* **13,** sc20181108–sc20181108,.

Patria, A. & Putra, P.S., 2020. Development of the Palu–Koro Fault in NW Palu Valley, Indonesia, *Geosci. Lett.,* **7**(1), 1–11,.

Prasetya, G.S., de Lange, W.P. & Healy, T.R., 2001. The Makassar Strait tsunamigenic region, Indonesia, *Nat. Hazards,* **24,** 295–307.

Puntodewo, S.S.O. *et al.*, 1994. GPS measurement of crustal deformation within the Pacific-Australia plate boundary Zone in Irian Jaya, Indonesia, *Tectonophysics,* **237,** 3-4, 141–153,.

PuSGeN, 2018. *Post-event Studies of The 28 September 2018 Earthquake in Palu, Central Sulawesi (Kajian Gempa Palu Provinsi Sulawesi Tengah, 28 September 2018 (M7.4)),* Pusat Perumahan dan Pemukiman, Balitbang PU.

PuSGeN, 2019. *Progress Report of Post-2018 earthquake Studies forf Mapping The Palukoro Fault Hazard Zone (Laporan Pemetaan Zona Rawan Bencana Sesar Palukoro Pasca Gempa P28 Septemberr 28 2018), Center For Research And Development For Housing, Agency for Research and Development,* Ministry of Public Works and Housing.

Shaw, J.H. & Suppe, J., 1996. Earthquake hazards of active blind-thrust faults under the central Los Angeles basin, California, *J. geophys. Res.: Solid Earth,* **101**(B4), 8623–8642.

Sieh, K. & Natawidjaja, D., 2000. Neotectonics of the Sumatran fault, Indonesia, *J. geophys. Res.,* **105**(B12), 28,295–228,326.

Silver, E.A., McCafrey, R. & Smith, R.B., 1983. Collision, rotation, and the initiation of the subduction in the evolution of the Sulawesi, Indonesia, *J. geophys. Res.: Solid Earth,* **88**(B11), 9407–9418.

Socquet, A., Hollingsworth, J., Pathier, E. & Bouchon, M., 2019. Evidence of supershear during the 2018 magnitude 7.5 Palu earthquake from space geodesy, *Nat. Geosci.,* **12**(3), 192–199.

Socquet, A., Simons, W., Vigny, C., McCafrey, R., Subarya, C., Sarsito, D., Ambrosius, B. & Spakman, W., 2006. Microblock rotations and fault coupling in SE Asia tripple junction (Sulawesi, Indonesia) from GPS and earthquake slip vector data, *J. geophys. Res.,* **111,** B8,.

Song, X., Zhang, Y., Shan, X., Liu, Y., Gong, W. & Qu, C., 2019. Geodetic observations of the 2018 Mw 7.5 Sulawesi earthquake and its implications for the kinematics of the Palu fault, *Geophys. Res. Lett.,* **46**(8), 4212–4220.

Stevens, C. *et al.*, 1999. Rapid rotations about a vertical axis in a collisional setting revealed by the Palu fault, Sulawesi, Indonesia, *Geeophys. Res. Lett.,* **26,** 2677–2680.

Supendi, P. *et al.*, 2020. Relocated aftershocks and background seismicity in eastern Indonesia shed light on the 2018 Lombok and Palu earthquake sequences, *Geophys. J. Int.,* **221,** 1845–1855.

Valkaniotis, S., Ganas, A., Tsironi, V. & Barberopoulou, A., 2018. *A Preliminary Report on the M7.5 Pau Earthquake Co-seismic Ruptures and Landslides using Image Correlation Techniques on Optical Satellite Data,* EMSC.

Walpersdorf, A., Vigny, C., Subarya, C. & Manurung, P., 1998. Monitoring of the Palu-Koro fault (Sulawesi) by GPS, *Geophys. Res. Lett.,* **25,** 2313–2316.

Wang, Y., Feng, W., Chen, K.M. & Samsonov, S.A., 2019. Source characteristics of 28 Septemberr 28 2018 Mw 7.4 Palu, Indonesia, earthquake derived from the advanced land observation satellite 2 data, *Remote. Sens.,* **11,** 1–16,.

Watkinson, I.M., Hall, R., Cummins, P.R. & Meilano, I., 2017. Active faults of eastern Indonesia, in *Geohazards in Indonesia: Earth Science for Disaster Risk Reduction,* Volume Special Publication, pp. 1–7, Geological Society of London.

Watkinson, I.M. & Hall, R., 2019. Impact of communal irrigation on the 2018 Palu earthquake-triggered landslides, *Nat. Geosci.,* **12**(11), 940–945.

Wells, D.L. & Coopersmith, K.J., 1994. New empirical relationships among magnitude, rupture length, rupture width, rupture area, and surface displacement, *Bull. seism. Soc. Am.,* **84**(4), 974–1002.

Wesnousky, S.G., 2006. Predicting endpoints of earthquake ruptures, *Nature,* **444,** 358–360.

Widiyantoro, S. & van der Hilst, R., 1997. Mantle structure beneath Indonesia inferred from high-resolution tomographic imaging, *Geophys. J. Int.,* **130**(1), 167–182.

Yeats, R.S., Sieh, K.E. & Allen, C.R., 1997. *The Geology of Earthquakes,* Oxford University Press, New York, **vi,** p. 568.